Journal of Scientific Computing (2023) 95:63
https://doi.org/10.1007/s10915-023-02198-2

A Second-order Time-Accurate Unconditionally Stable Method for a Gradient Flow for the Modica–Mortola Functional

Seokjun Ham[1] · **Soobin Kwak**[1] · **Chaeyoung Lee**[1] · **Gyeonggyu Lee**[1] · **Junseok Kim**[1]

Received: 14 October 2022 / Revised: 10 February 2023 / Accepted: 28 March 2023 /

Abstract

In this study, we present a second-order time-accurate unconditionally stable numerical method for a gradient flow for the Modica–Mortola functional with an equispaced multiple well potential. The proposed second-order time-accurate unconditionally stable numerical method is based on the operator splitting method. The nonlinear and linear terms in the gradient flow are solved analytically and using the Fourier spectral method, respectively. The numerical solutions in each step are bounded for any time step size and the overall scheme is temporally second-order accurate. We prove theoretically the unconditional stability and boundedness of the numerical solutions. In addition, several numerical tests are conducted to demonstrate the performance of the proposed method.

Keywords Modica–Mortola functional · Fourier spectral method · Unconditionally stable scheme

Mathematics Subject Classification 65M06 · 65M12 · 35B99

1 Introduction

In this study, we present a temporally second-order unconditionally stable numerical method for a gradient flow for the Modica–Mortola (MM) functional with an equispaced multiple well potential:

$$\frac{\partial \phi(\mathbf{x},t)}{\partial t} = -\frac{\pi}{\epsilon}\sin\big(2\pi\phi(\mathbf{x},t)\big) + 2\epsilon\Delta\phi(\mathbf{x},t), \tag{1}$$

$$\mathbf{n}\cdot\nabla\phi = 0 \text{ on } \partial\Omega, \tag{2}$$

✉ Junseok Kim
cfdkim@korea.ac.kr

[1] Department of Mathematics, Korea University, Seoul 02841, Republic of Korea

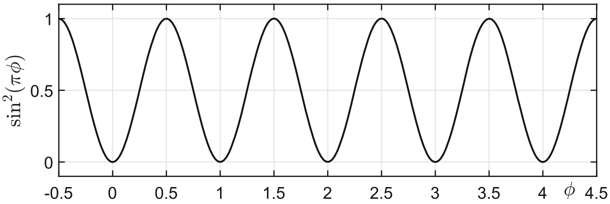

Fig. 1 $\sin^2(\pi\phi)$ on $[-0.5,\ 4.5]$

where $\phi(\mathbf{x}, t)$ is an order parameter in space $\mathbf{x} \in \Omega$ and time t, ϵ is a parameter which is related to the thickness of the interfacial transition layer, $\mathbf{n}$ is the unit normal vector to the domain boundary $\partial\Omega$. Equation (1) is a gradient flow for the MM functional [10]:

$$\mathcal{E}(\phi) := \int_\Omega \left[\frac{1}{\epsilon} \sin^2(\pi\phi) + \epsilon|\nabla\phi|^2 \right] d\mathbf{x}, \tag{3}$$

where $(1/\epsilon)\sin^2(\pi\phi)$ is the multiple periodic well potential, see Fig. 1.

Phase-field models have been extensively researched in various fields such as geometric surface [19] and interface [1], materials science [3, 18, 20], dynamics of fluid flow [4, 5, 22], and image process [2, 7, 16], etc. The multi-phase image segmentation was introduced using phase-field model [2, 16]. An explicit time-stepping scheme to construct pattern formation in reaction-diffusion systems on evolving surfaces is proposed [11]. Rong et al. [21] proposed an adaptive method using total variation–Allen–Cahn type for multi-phase image segmentation. The parallel algorithms for crystal evolution were introduced using a multi-physics phase-field framework [7]. Giga et al. [3] investigated the singular limit of single-well MM functional under Hausdorff distance of graphs convergence. They presented an explicit representation of Kobayashi–Warren–Carter energy. Jin et al. [8] proposed a numerical method for electrical impedance tomography. They took an MM-type functional that has double-well potential to treat the adaptive finite element method (FEM). Ma et al. [18] presented a high order method of a fast Fourier-transform based to solve multi-phase-field models in a periodic domain. Second-order energy stable schemes were proposed for viscous fluid mixtures [4, 5, 22]. Li et al. [14] developed and analyzed a temporally second-order unconditionally stable FEM for solving the Allen–Cahn (AC) equation. A high-order energy stable scheme for the conservative AC equation with non local Lagrange multiplier by combining the concept of energy quadratization and the Runge–Kutta method[13]. A parabolic sine-Gordon equation of phase-field model was solved with a temporally second-order accurate unconditionally stable method [6]. Zhang et al. performed energy stability analysis for stabilized semi-implicit scheme for Cahn–Hilliard equation. Zheng and Li [24] proposed scalar auxiliary variable scheme based on the Fourier spectral method for Cahn–Hilliard–Hele–Shaw system and derived unconditional energy stability.

Li and Kim [17] proposed a phase-field model for multiphase image segmentation using periodic quartic polynomial as a potential energy. The proposed phase-field model was implicitly solved using the operator splitting method (OSM) with a multigrid method and closed-form solution. Li et al. [16] presented a gradient flow equation of the MM functional for multiphase image segmentation. They used an explicit Euler method to solve the presented equation. Therefore, the presented numerical method has time step restriction. In this paper, we use gradient flow of the MM functional which has multiple-well potentials to represent multi-phase solutions. By using the Strang-type splitting method, we obtain second-order accurate approximations for a gradient flow for the MM functional. The main difficulty of this work is to find a closed-form solution for periodic nonlinear term in the gradient flow of the MM functional. It makes the proposed numerical method accurate and stable. By the boundedness of the numerical solutions, we show the unconditional stability of the proposed scheme.

The contents of this paper are as follows. In Sect. 2, the numerical solution algorithm is described. In Sect. 4, the numerical experiments are presented. In Sect. 3, unconditional stability and boundedness of the proposed numerical method are proved. In Sect. 5, the conclusions are given.

2 Numerical Solution Algorithm

In this section, we describe the temporally second-order unconditionally stable numerical method for a gradient flow for the MM functional with an equispaced multiple well potential in two-dimensional (2D) space. We numerically solve Eq. (1) in $\Omega = (L_x, R_x) \times (L_y, R_y)$. Let us discretize the computational domain as $\Omega_h = \{(x_i, y_j) : x_i = L_x + (i - 0.5)h,\ y_j = L_y + (j - 0.5)h,\ |\ 1 \le i \le N_x,\ 1 \le j \le N_y\}$, where N_x, N_y be integers and $h = (R_x - L_x)/N_x$ be the grid size. Let $\phi_{ij}^n := \phi(x_i, y_j, n\Delta t)$, where Δt is the time step. To numerically solve Eq. (1), we use the OSM and rewrite it as

$$\frac{\partial \phi(\mathbf{x}, t)}{\partial t} = \mathcal{N}\big(\phi(\mathbf{x}, t)\big) + \mathcal{L}\big(\phi(\mathbf{x}, t)\big), \tag{4}$$

where $\mathcal{N}\big(\phi(\mathbf{x}, t)\big) = -(\pi/\epsilon)\sin\big(2\pi\phi(\mathbf{x}, t)\big)$ and $\mathcal{L}\big(\phi(\mathbf{x}, t)\big) = 2\epsilon\Delta\phi(\mathbf{x}, t)$. Then, a second-order OSM [12] is as follows: We solve Eq. (5) with $\psi_1(\mathbf{x}, 0) = \phi(\mathbf{x}, n\Delta t)$ for a given value $\phi(\mathbf{x}, n\Delta t)$ to get $\psi_1(\mathbf{x}, \Delta t/2)$.

$$\frac{\partial \psi_1(\mathbf{x}, t)}{\partial t} = \mathcal{N}\big(\psi_1(\mathbf{x}, t)\big). \tag{5}$$

Then, using $\psi_1(\mathbf{x}, \Delta t/2)$, we solve Eq. (6) with $\psi_2(\mathbf{x}, 0) = \psi_1(\mathbf{x}, \Delta t/2)$ to get $\psi_2(\mathbf{x}, \Delta t)$.

$$\frac{\partial \psi_2(\mathbf{x}, t)}{\partial t} = \mathcal{L}\big(\psi_2(\mathbf{x}, t)\big). \tag{6}$$

Analogously, using $\psi_2(\mathbf{x}, \Delta t)$, we solve (7) with $\psi_3(\mathbf{x}, 0) = \psi_2(\mathbf{x}, \Delta t)$ to get $\psi_3(\mathbf{x}, \Delta t/2)$.

$$\frac{\partial \psi_3(\mathbf{x}, t)}{\partial t} = \mathcal{N}\big(\psi_3(\mathbf{x}, t)\big). \tag{7}$$

Finally, we set $\phi(\mathbf{x}, (n + 1)\Delta t) = \psi_3(\mathbf{x}, \Delta t/2)$.

Now, we describe its steps in detail. First, we consider Eq. (5) with an initial condition $\psi_1(\mathbf{x}, 0) = \phi(\mathbf{x}, n\Delta t)$.

$$\frac{\partial \psi_1(\mathbf{x}, t)}{\partial t} = -\frac{\pi}{\epsilon}\sin\big(2\pi\psi_1(\mathbf{x}, t)\big). \tag{8}$$

Equation (8) has an analytic solution and Fig. 2 schematically shows $-(\pi/\epsilon)\sin(2\pi v)$ term in Eq. (8).

If $\sin\big(2\pi\psi_1(\mathbf{x}, t)\big) = 0$, then

$$\psi_1(\mathbf{x}, t) = \psi_1(\mathbf{x}, 0). \tag{9}$$

Otherwise, $\sin\big(2\pi\psi_1(\mathbf{x}, t)\big) \neq 0$, we can rewrite Eq. (8) in the form as

$$\frac{d\psi_1}{\sin(2\pi\psi_1)} = -\frac{\pi}{\epsilon}dt. \tag{10}$$

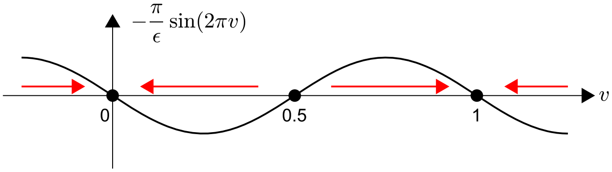

Fig. 2 $-\frac{\pi}{\epsilon}\sin(2\pi v)$ respect to v

For simplicity of the notation, we omitted the argument ($\mathbf{x}$,t). Multiplying by $\sin(2\pi\psi_1)$ on both the denominator and numerator of the left-hand side of Eq. (10) by, we have

$$\frac{\sin(2\pi\psi_1)}{\sin^2(2\pi\psi_1)}d\psi_1 = -\frac{\pi}{\epsilon}dt. \tag{11}$$

Using the Pythagorean trigonometric identity, we have

$$\frac{\sin(2\pi\psi_1)}{1-\cos^2(2\pi\psi_1)}d\psi_1 = -\frac{\pi}{\epsilon}dt. \tag{12}$$

Then, by using partial fraction expansion on the left side and integrating both sides, we obtain

$$\int \frac{1}{2}\left(\frac{\sin(2\pi\psi_1)}{1+\cos(2\pi\psi_1)} + \frac{\sin(2\pi\psi_1)}{1-\cos(2\pi\psi_1)}\right)d\psi_1 = -\int \frac{\pi}{\epsilon}dt, \tag{13}$$

which results in

$$\frac{1}{4\pi}\ln\frac{1-\cos(2\pi\psi_1)}{1+\cos(2\pi\psi_1)} = -\frac{\pi}{\epsilon}t + C(\mathbf{x}), \tag{14}$$

where

$$C(\mathbf{x}) = \frac{1}{4\pi}\ln\frac{1-\cos\big(2\pi\psi_1(\mathbf{x},0)\big)}{1+\cos\big(2\pi\psi_1(\mathbf{x},0)\big)}. \tag{15}$$

The solution to Eq. (14) is given as

$$\begin{aligned}\psi_1(\mathbf{x},t) = \; & \lfloor\phi(\mathbf{x},n\Delta t)\rfloor + \frac{1+\operatorname{sgn}(\bar{\phi}(\mathbf{x},n\Delta t)-0.5)}{2} \\ & + \frac{\operatorname{sgn}\big(0.5-\bar{\phi}(\mathbf{x},n\Delta t)\big)}{2\pi}\cos^{-1}\left(\frac{1-e^{-\frac{4\pi^2}{\epsilon}t+4\pi C(\mathbf{x})}}{1+e^{-\frac{4\pi^2}{\epsilon}t+4\pi C(\mathbf{x})}}\right),\end{aligned} \tag{16}$$

where

$$C(\mathbf{x}) = \frac{1}{4\pi}\ln\frac{1-\cos\big(2\pi\phi(\mathbf{x},\Delta t)\big)}{1+\cos\big(2\pi\phi(\mathbf{x},\Delta t)\big)} \quad \text{and} \quad \bar{\phi}(\mathbf{x},\Delta t) = \phi(\mathbf{x},\Delta t) - \lfloor\phi(\mathbf{x},n\Delta t)\rfloor.$$

Here, $\operatorname{sgn}(x)$ is the sign function and $\lfloor x\rfloor$ is the floor function i.e., $\lfloor x\rfloor = \max\{m\in\mathbb{Z}\,|\,m\le x\}$. Now, using the analytic solution form (16), we can obtain $\psi_1(\mathbf{x},\Delta t/2)$.

Next, we solve Eq. (6)

$$\frac{\partial\psi_2(\mathbf{x},t)}{\partial t} = 2\epsilon\Delta\psi_2(\mathbf{x},t), \tag{17}$$

using the Fourier spectral method with an initial condition $\psi_2(\mathbf{x},0) = \psi_1(\mathbf{x},\Delta t/2)$. To apply the homogeneous Neumann boundary condition (2), we use the discrete cosine transform.

For the given data $\{u(x_i, y_j)|i = 1, \cdots, N_x \text{ and } j = 1, \cdots, N_y\}$, the discrete cosine transform is defined as follows:

$$\hat{u}(p,q) = \alpha_p \beta_q \sum_{i=1}^{N_x} \sum_{j=1}^{N_y} u(x_i, y_j) \cos\big(\xi_p \pi (x_i - L_x)\big) \cos\big(\eta_q \pi (y_j - L_y)\big)$$

for $p = 0, \ldots, N_x - 1$ and $q = 0, \ldots, N_y - 1$. The inverse discrete cosine transform is

$$u(x_i, y_j) = \sum_{p=1}^{N_x} \sum_{q=1}^{N_y} \alpha_p \beta_q \hat{u}(p,q) \cos\big(\xi_p \pi (x_i - L_x)\big) \cos\big(\eta_q \pi (y_j - L_y)\big), \tag{18}$$

where

$$\alpha_p = \begin{cases} \sqrt{\frac{1}{N_x}} & (p = 1) \\ \sqrt{\frac{2}{N_x}} & (p \geq 2) \end{cases}, \quad \beta_q = \begin{cases} \sqrt{\frac{1}{N_y}} & (q = 1) \\ \sqrt{\frac{2}{N_y}} & (q \geq 2) \end{cases} \tag{19}$$

and $\xi_p = (p-1)/(R_x - L_x)$, $\eta_q = (q-1)/(R_y - L_y)$. Let us assume that

$$\psi_2(x_i, y_j, t) = \sum_{p=1}^{N_x} \sum_{q=1}^{N_y} \alpha_p \beta_q \hat{\psi}_2(p,q,t) \cos\big(\xi_p \pi (x_i - L_x)\big) \cos\big(\eta_q \pi (y_j - L_y)\big). \tag{20}$$

Applying Eq. (20) in Eq. (17), we have

$$\frac{d\hat{\psi}_2(p,q,t)}{dt} = -2\epsilon[\big(\xi_p \pi\big)^2 + \big(\eta_q \pi\big)^2]\hat{\psi}_2(p,q,t). \tag{21}$$

Hence, in the Fourier space, the solution of Eq. (21) is given as

$$\begin{aligned} \hat{\psi}_2(p,q,t) &= \hat{\psi}_2(p,q,0) e^{-2\epsilon t[(\xi_p \pi)^2 + (\eta_q \pi)^2]} && (22) \\ &= \hat{\psi}_1(p,q,\Delta t/2) e^{-2\epsilon t[(\xi_p \pi)^2 + (\eta_q \pi)^2]}. && (23) \end{aligned}$$

Applying the inverse discrete cosine transform (18), the solution of Eq. (17) is obtained:

$$\psi_2(x_i, y_j, t) = \sum_{p=1}^{N_x} \sum_{q=1}^{N_y} \alpha_p \beta_q \hat{\psi}_2(p,q,t) \cos\big(\xi_p \pi (x_i - L_x)\big) \cos\big(\eta_q \pi (y_j - L_y)\big). \tag{24}$$

As a last step, we consider the last operator in Eq. (7) with $\psi_3(\mathbf{x}, 0) = \psi_2(\mathbf{x}, \Delta t)$. Equation (7) also can be solved analogously as (16):

$$\begin{aligned} \psi_3(\mathbf{x}, t) = {} & \lfloor \psi_2(\mathbf{x}, n\Delta t) \rfloor + \frac{1 + \text{sgn}(\bar{\psi}_2(\mathbf{x}, n\Delta t) - 0.5)}{2} \\ & + \frac{\text{sgn}\big(0.5 - \bar{\psi}_2(\mathbf{x}, n\Delta t)\big)}{2\pi} \cos^{-1}\left(\frac{1 - e^{-\frac{4\pi^2}{\epsilon}t + 4\pi C(\mathbf{x})}}{1 + e^{-\frac{4\pi^2}{\epsilon}t + 4\pi C(\mathbf{x})}} \right), \end{aligned} \tag{25}$$

where

$$C(\mathbf{x}) = \frac{1}{4\pi} \ln \frac{1 - \cos\big(2\pi \psi_2(\mathbf{x}, \Delta t)\big)}{1 + \cos\big(2\pi \psi_2(\mathbf{x}, \Delta t)\big)} \quad \text{and} \quad \bar{\psi}_2(\mathbf{x}, \Delta t) = \psi_2(\mathbf{x}, \Delta t) - \lfloor \psi_2(\mathbf{x}, n\Delta t) \rfloor.$$

Finally, we get $\phi(\mathbf{x}, (n+1)\Delta t) = \psi_3(\mathbf{x}, \Delta t/2)$.

3 Numerical Analysis

In this section, we prove that the proposed method is unconditionally stable and bounded in a step-by-step manner. For $1 \leq i \leq N_x$ and $1 \leq j \leq N_y$, we suppose that numerical solution of n-th time $\phi(x_i, y_j, n\Delta t)$ is bounded by some integers $N_{\min}$ and $N_{\max}$, i.e.,

$$N_{\min} \leq \phi(x_i, y_j, n\Delta t) \leq N_{\max}, \tag{26}$$

where $N_{\min} = \min\{\lfloor \phi(x_i, y_j, n\Delta t) \rfloor | 1 \leq i \leq N_x,\ 1 \leq j \leq N_y\} - 1$ and $N_{\max} = \max\{\lceil \phi(x_i, y_j, n\Delta t) \rceil | 1 \leq i \leq N_x,\ 1 \leq j \leq N_y\} + 1$. Here, $\lfloor x \rfloor$ and $\lceil x \rceil$ are floor and ceiling functions, respectively.

In the first step (5), for each i and j, we take m_{ij} as $m_{ij} \leq \phi(x_i, y_j, n\Delta t) < m_{ij} + 1$, where $m_{ij} = \lfloor \phi(x_i, y_j, n\Delta t) \rfloor$. Here, m_{ij} satisfies $N_{\min} + 1 \leq m_{ij} < N_{\max} - 1$. If $\phi(x_i, y_j, n\Delta t) = N_{\max} - 1$ for some i and j, then $\psi_1(x_i, y_j, t) = N_{\max} - 1$ for any time t from Eq. (16). From Eq. (16), we consider following three cases for each i and j as follows: $\bar{\psi}_1(x_i, y_j, \Delta t/2) < 0.5$, $\bar{\psi}_1(x_i, y_j, \Delta t/2) = 0.5$, and $\bar{\psi}_1(x_i, y_j, \Delta t/2) > 0.5$. Using the condition $0 < \cos^{-1}\left(\frac{1 - e^{-\frac{4\pi^2}{\epsilon}t + 4\pi C(\mathbf{x})}}{1 + e^{-\frac{4\pi^2}{\epsilon}t + 4\pi C(\mathbf{x})}}\right) < \pi$ and Eq. (16), we can derive the following equation and inequalities for the three cases from Eq. (16):

$$\begin{cases} m_{ij} \leq \psi_1(x_i, y_j, t) < m_{ij} + 0.5, & \text{if} \quad \bar{\phi}(x_i, y_j, n\Delta t) < 0.5, \\ \psi_1(x_i, y_j, t) = m_{ij} + 0.5, & \text{if} \quad \bar{\phi}_1(x_i, y_j, n\Delta t) = 0.5, \\ m_{ij} + 0.5 < \psi_1(x_i, y_j, t) < m_{ij} + 1, & \text{if} \quad \bar{\phi}(x_i, y_j, n\Delta t) > 0.5. \end{cases} \tag{27}$$

Therefore, the solution $\psi_1(x_i, y_j, t)$ is bounded for any $t > 0$:

$$m_{ij} \leq \psi_2(x_i, y_j, t) < m_{ij} + 1.$$

Because $N_{\min} < m_{ij}$ and $m_{ij} + 1 < N_{\max}$, ψ_2 is also bounded as

$$N_{\min} < \psi_2(x_i, y_j, t) < N_{\max}$$

for any time t.

In the second step (6), the initial condition is obtained as $\psi_2(x, y, 0) = \psi_1(x, y, \Delta t/2)$. We denote that $\Psi_2(x, y, 0)$ is a continuous representation of the smooth numerical solution $\psi_2(x_i, y_j, 0)$ by using discrete cosine transform as follows:

$$\Psi_2(x, y, 0) = \sum_{p=1}^{N_x} \sum_{q=1}^{N_y} \alpha_p \beta_q \hat{\psi}_2(p, q, 0) \cos\left(\xi_p \pi (x - L_x)\right) \cos\left(\eta_q \pi (y - L_y)\right), \tag{28}$$

which also satisfies the solution for the discrete points x_i and y_j for $1 \leq i \leq N_x$ and $1 \leq j \leq N_y$. Then, the continuous representation of an initial condition $\Psi_2(x, y, n\Delta 0)$ is bounded by $N_{\min}$ and $N_{\max}$, i.e.,

$$N_{\min} \leq \Psi_2(x_i, y_j, 0) \leq N_{\max}. \tag{29}$$

The boundedness of continuous representation in Eq. (29) guarantees the following boundedness of numerical solution.

$$N_{\min} \leq \psi_2(x_i, y_j, 0) \leq N_{\max}. \tag{30}$$

Substituting Eq. (23) into Eq. (24),

$$\psi_2(x_i, y_j, t) = \sum_{p=1}^{N_x}\sum_{q=1}^{N_y} \alpha_p \beta_q \hat{\psi}_2(p, q, 0) e^{-2\epsilon t[(\xi_p \pi)^2 + (\eta_q \pi)^2]} \cos(\xi_p \pi x_i)\cos(\eta_q \pi y_j). \tag{31}$$

In Eq. (31), $\psi_2(x_i, y_j, t)$ is a solution of the heat equation with the initial condition $\psi_2(x_i, y_j, 0) = \psi_1(x_i, y_j, \Delta t/2)$. The numerical solution of the heat equation using Fourier spectral method with the zero Neumann boundary condition satisfies the discrete maximum and minimum principle:

$$N_{\min} \le \min_{ij} \Psi_2(x, y, 0) \le \psi_2(x_i, y_j, t) \le \max_{ij} \Psi_2(x, y, 0) \le N_{\max}, \tag{32}$$

which results in $N_{\min} \le \psi_2(x_i, y_j, t) \le N_{\max}$ for any time $t > 0$. In particular, $N_{\min} \le \psi_2(x_i, y_j, \Delta t) \le N_{\max}$.

In the third step (7), because $\psi_3(x_i, y_j, 0) = \psi_2(x_i, y_j, \Delta t)$ is bounded by $N_{\min}$ and $N_{\max}$ for any time t, the following inequality holds using the similar procedure used in the first step:

$$N_{\min} \le \psi_3(x_i, y_j, t) \le N_{\max}. \tag{33}$$

Finally, ϕ_{ij}^{n+1} is obtained as $\phi(x_i, y_j, n\Delta t) = \psi_3(x_i, y_j, \Delta t/2)$, for $n = 0, 1, 2, \cdots$. Hence, the proposed scheme is unconditionally stable and the numerical solutions are bounded below and above by $N_{\min}$ and $N_{\max}$, respectively, for any time step size, which implies the boundedness of the computational solutions.

4 Numerical Experiments

Now, we perform numerical experiments for the gradient flow of MM functional using the operator splitting scheme. Unless otherwise noted, we use numerical parameters as $N_x = 128$, and $h = 2/N_x$ for grid points of the uniform spatial discretization to one-dimensional computational domain $\Omega = (-1, 1)$. In two-dimensional computational domain $\Omega = (-1, 1)^2$, we use numerical parameter as $N_x = N_y = 128$ and $h = 2/N_x = 2/N_y$ for the uniform spatial discretization.

4.1 Estimation of ϵ

First, we define a thickness of the interfacial transition layer as $L = |x_2 - x_1|$, where $\phi(x_1) = 0.05$ and $\phi(x_2) = 0.95$ in one-dimensional space as illustrated in Fig. 3.

To investigate a convergence of the interfacial transition layer, we consider the following two different initial conditions,

$$\phi_1(x, 0) = \frac{1}{2}(x + 1), \tag{34}$$

$$\phi_2(x, 0) = \begin{cases} 0, & \text{if } x < 0, \\ 1, & \text{otherwise,} \end{cases} \tag{35}$$

in the computational domain $\Omega = (-1, 1)$. We assume that ϕ^n is a numerical equilibrium solution if $||\phi^n - \phi^{n-1}||_2 < 10^{-6}$, here the tolerance is 10^{-6}. Figure 4 shows that the two equilibrium solutions ϕ_1^n and ϕ_2^n, which have two different initial conditions, coincide.

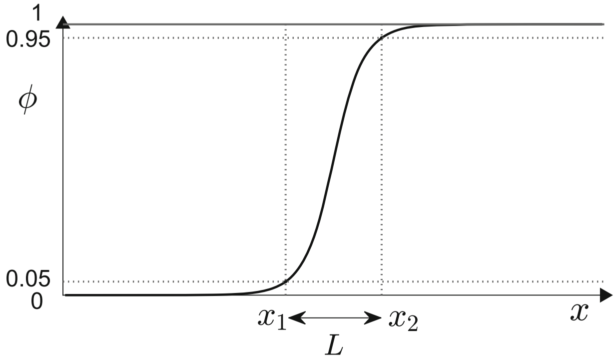

Fig. 3 Schematic for thickness of interfacial transition layer

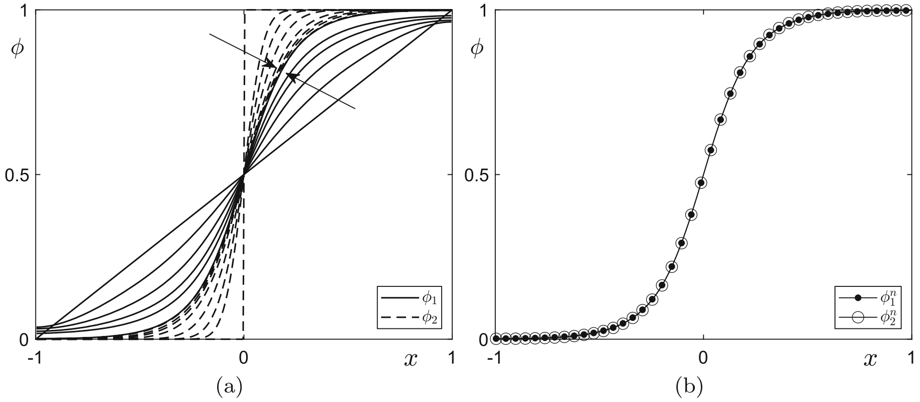

(a) (b)

Fig. 4 **a** Snapshots and **b** equilibrium solutions of ϕ_1 and ϕ_2 with $\Delta t = 0.5\,h^2$, $N_x = 256$, and $\epsilon = 60h$

Table 1 Thickness of the interface transition layer with various ϵ values. Here, $N_x = 256$, $h = 2/N_x$, and $\Delta t = 0.1h^2$

Case	$\epsilon = 2h$	$\epsilon = 4h$	$\epsilon = 6h$	$\epsilon = 8h$	$\epsilon = 10h$	$\epsilon = 12h$
Thickness(L)	$3.2254h$	$6.6192h$	$9.8478h$	$12.9754h$	$16.2875h$	$19.5066h$

Then, we estimate the relation between ϵ and thickness of the interfacial transition layer. Table 1 lists the thickness of the interface layer of equilibrium solution for various ϵ values. In this case, we take $\phi_2(x, 0)$ in Eq. (34) as the initial condition. We use the linear interpolation to find x_1 and x_2, which satisfy $\phi(x_1) = 0.05$ and $\phi(x_2) = 0.95$. Then we obtain thickness as $L = |x_2 - x_1|$.

For convenience of calculation, we want to derive a formula $\epsilon(m, h) = amh$ which can have a given interface thickness L if $\epsilon = \epsilon(m, h)$, where $m = L/h$. By least-square curve fitting to the data in Table 1 as a linear function through the origin, we can estimate $\epsilon(m, h)$ using the following linear equation:

$$\epsilon(m, h) = 0.61405mh. \tag{36}$$

In Fig. 5, data given from Table 1 and the corresponding linear fitted function are illustrated.

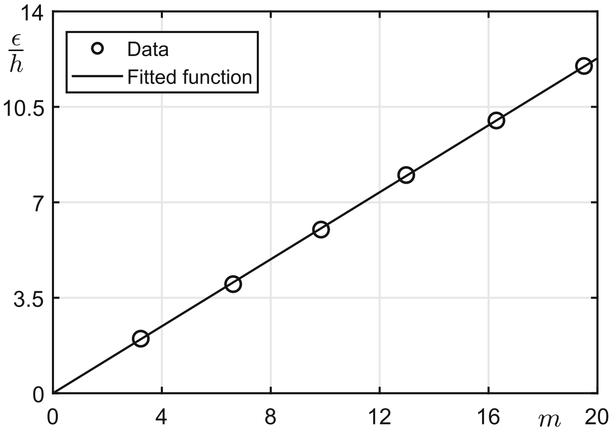

Fig. 5 Linear fitting function of $\epsilon/h = am$ respect to m, where $a = 0.61405$

4.2 Stability Test

We test the numerical stability and boundedness of the proposed scheme for the gradient flow of MM functional in two-dimensional space in Figs. 6 and 7. In two-dimensional computational domain $(-1, 1) \times (-1, 1)$, we use $\epsilon = \epsilon(5, h)$, $h = 2/128$, and an initial condition

$$\phi(x, y, 0) = \frac{1}{2}(x + 1)^2 + (y + 1)^2 + \text{rand}(x, y), \tag{37}$$

where ‘rand(x, y)’ is uniformly distributed random number between -0.5 and 0.5. The initial condition (37) has random perturbation between -0.5 and 0.5 as shown in the first columns of Fig. 6. Figures 6(a)–(c) illustrate the temporal dynamics of two-dimensional gradient flow of MM functional with three different time steps $\Delta t_1 = 0.01\,h^2$, $\Delta t_2 = h^2$, and $\Delta t_3 = 100\,h^2$, respectively. The last column of Figs. 6(a)–(c) are the numerical solutions up to time $t = 0.0244$, $t = 0.0244$, and $t = 0.0488$, respectively. The solution does not blow up with a large time step as $\Delta t_3 = 100h^2$ and seems consistent with solutions using small time steps.

To validate the pointwise boundedness of numerical solutions, we define discrete maximum and minimum as follows:

$$\phi_{\max} = \max_{1 \le i \le N_x, 1 \le j \le N_y} \phi_{ij}, \tag{38}$$

$$\phi_{\min} = \min_{1 \le i \le N_x, 1 \le j \le N_y} \phi_{ij}. \tag{39}$$

Fig. 7 shows a temporal evolution of maximum and minimum values for the numerical solutions with the random initial condition (37) up to time $t = 0.0244$. As shown in Fig. 7, the maximum and minimum values of the solutions are bounded by $N_{\max}$ and $N_{\min}$ for all three different time steps $\Delta t_1 = 0.01\,h^2$, $\Delta t_2 = h^2$, and $\Delta t_3 = 100h^2$. From the result in Fig. 7, it is confirmed that the numerical solutions are bounded by $N_{\min}$ and $N_{\max}$ point-wisely for several time step sizes.

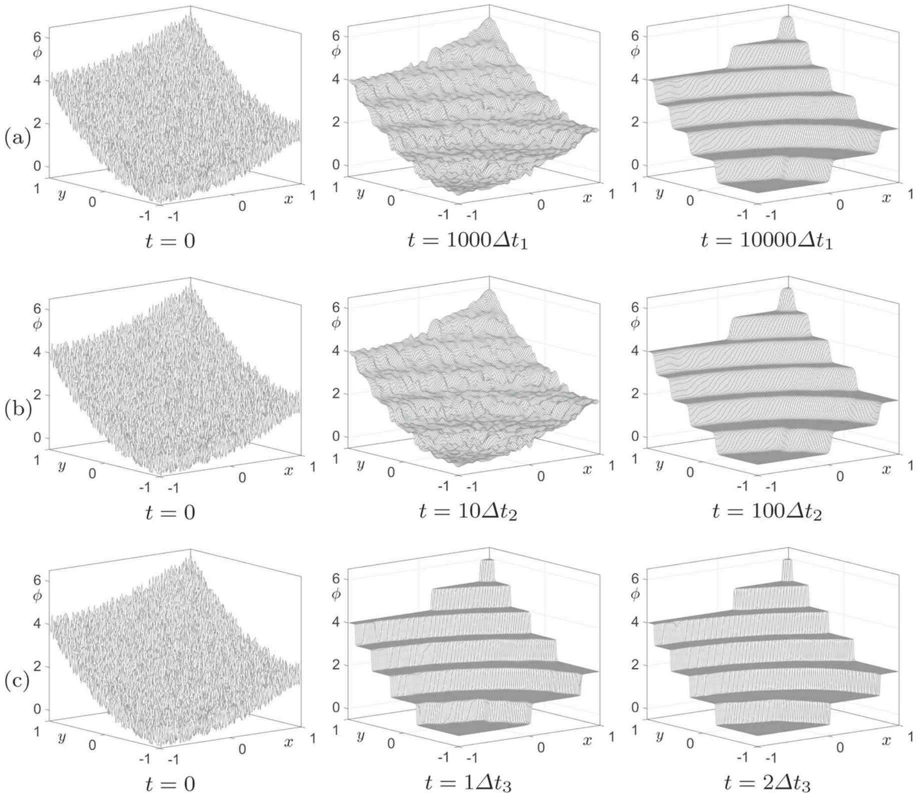

$t = 0$ $t = 1000\Delta t_1$ $t = 10000\Delta t_1$

$t = 0$ $t = 10\Delta t_2$ $t = 100\Delta t_2$

$t = 0$ $t = 1\Delta t_3$ $t = 2\Delta t_3$

Fig. 6 Snapshots of temporal dynamics of two-dimensional gradient flow for the MM functional using different time steps as **a** $\Delta t_1 = 0.01h^2$, **b** $\Delta t_2 = h^2$, and **c** $\Delta t_3 = 100\,h^2$

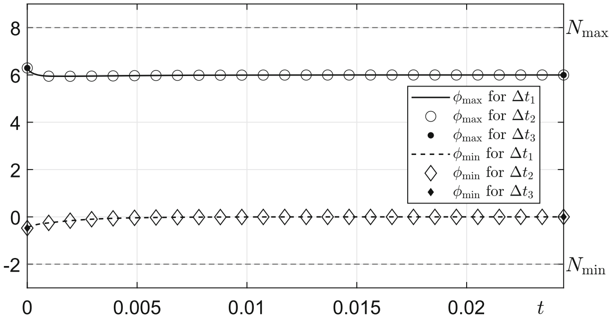

Fig. 7 Temporal evolution of maximum and minimum values for the numerical solutions with three different time steps $\Delta t_1 = 0.01\,h^2$, $\Delta t_2 = h^2$, and $\Delta t_3 = 100\,h^2$

4.3 Convergence Test

In this section, We numerically demonstrate that the numerical scheme described in Sect. 2 is temporally second-order accurate and spatially spectral-order accurate in space. For the

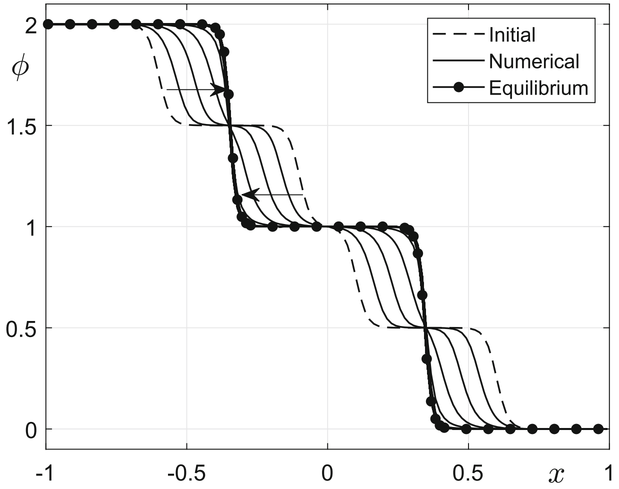

Fig. 8 Temporal evolution of Eq. (40) at $y = h$

Table 2 Errors and rates of convergence in time

$(\Delta t, \Delta t/2)$	Error	Rate
(1.00e−4, 5.00e−5)	2.5839e−7	
(5.00e−5, 2.50e−5)	6.4592e−8	2.00
(2.50e−5, 1.25e−5)	1.6157e−8	2.00
(1.25e−5, 6.25e−6)	4.0655e−9	1.99

test, the initial condition is defined as follows:

$$\phi(x, y, 0) = 0.25\left[4 - \tanh\left(\frac{x+0.6}{0.04}\right) - \tanh\left(\frac{x+0.1}{0.04}\right) - \tanh\left(\frac{x-0.1}{0.04}\right) - \tanh\left(\frac{x-0.6}{0.04}\right)\right], \tag{40}$$

on $\Omega = (-1, 1)^2$. Figure 8 shows the initial, numerical, and equilibrium solutions of Eq. (40) at $y = h$. Here, we use $N_x = N_y = 128$, $h = 2/N_x$, $\Delta t = 1.0\text{e-}4$, and $\epsilon = 0.048$.

We first fix the final time to $T = N_t \Delta t = 0.002$, where N_t is a non-negative integer, and then observe the consecutive l_2-norm errors while decreasing Δt by half for the rate of convergence in time. The discrete l_2-norm error is defined as

$$||\text{Error}^{(\Delta t, \Delta t/2)}||_2 = \sqrt{\sum_{i=1}^{N_x}\sum_{j=1}^{N_y} \frac{1}{N_x N_y}\left(\phi_{ij}^{N_t} - \phi_{ij}^{2N_t}\right)^2},$$

and the rate of convergence is $\log_2(||\text{Error}^{(\Delta t, \Delta t/2)}||_2/||\text{Error}^{(\Delta t/2, \Delta t/4)}||_2)$. Table 2 lists the discrete l_2-norm errors and the rates of convergence in time, and confirms the proposed method is second-order accurate in time.

Next, to verify the spectral-order of accuracy in space, we fix the time step size to $\Delta t = 1.0\text{e-}6$ and the final time to $T = 10\Delta t$. While increasing the number of grids twice, we observe the discrete l_2-norm errors between two grids, coarse and fine. Here, Φ_{ij}^n and ϕ_{ij}^n

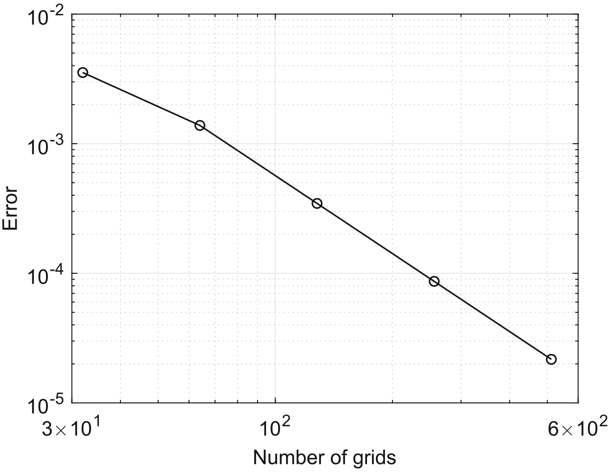

Fig. 9 Discrete l_2-norm errors with respect to the number of grid $N = N_x = N_y$

denote the numerical solutions of the coarse and fine grids at time $n\Delta t$, respectively. The number of fine grids is twice the number of coarse grids, $N = N_x = N_y$, and the size of one coarse grid is $h/2$, which is half the size of the coarse grid. We use $N = 32,\ 64,\ \ldots,\ 512$ and $h = 2/N$, and the discrete l_2-norm error is defined as

$$||\text{Error}_{(N,2N)}||_2 = \sqrt{\sum_{i=1}^{N_x}\sum_{j=1}^{N_y}\frac{1}{N_xN_y}\left(\Phi_{ij}^{N_t} - \frac{1}{4}(\phi_{2i-1,2j-1}^{N_t} + \phi_{2i-1,2j}^{N_t} + \phi_{2i,2j-1}^{N_t} + \phi_{2i,2j}^{N_t})\right)^2}.$$

Fig. 9 shows the discrete l_2-norm errors according to the number of grid N.

4.4 Motion by Mean Curvature

In this section, we investigate the mean curvature flow of the gradient flow for the MM functional in two-dimensional computational domain $\Omega = (-1, 1)^2$, with the interfacial transition parameter $\epsilon = \epsilon(5, h)$. We consider the following equation in the form of both sides of the original equation (1) divided by 2ϵ.

$$\frac{\phi_t}{2\epsilon} = -\frac{\pi}{2\epsilon^2}\sin\left(2\pi\phi(\mathbf{x}, t)\right) + \Delta\phi(\mathbf{x}, t). \tag{41}$$

We discretize Eq. (41) as

$$\frac{\phi_{ij}^{n+1} - \phi_{ij}^n}{\Delta\tau} = -\frac{\pi}{2\epsilon^2}\sin(2\pi\phi_{ij}^n) + \Delta\phi_{ij}^n, \tag{42}$$

where τ is a scaled time $\tau = n\Delta\tau$ and $\Delta\tau$ is a scaled time step as $\Delta\tau = 2\epsilon\Delta t$. Then we obtain the solution by using the proposed second-order accurate method in Sect. 2. In Fig. 10, we consider an initial condition,

$$\phi(x, y, 0) = \left[\tanh\left(\frac{R_0 - \sqrt{x^2 + y^2}}{\sqrt{2}\epsilon}\right) + 1\right]\Big/2, \tag{43}$$

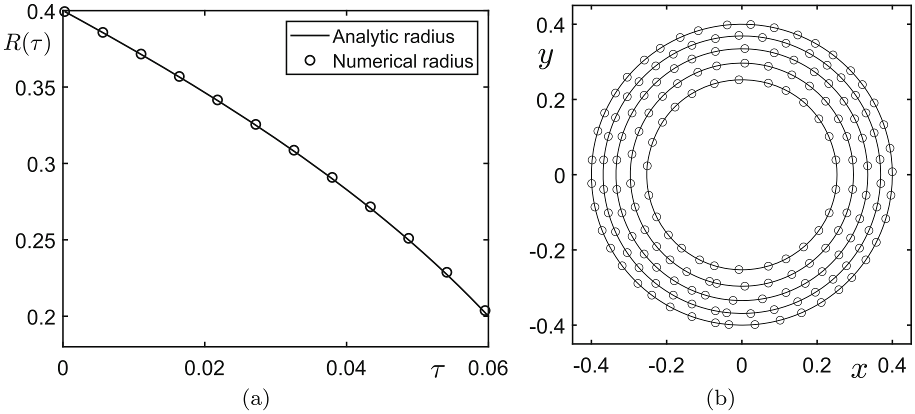

Fig. 10 (a) Comparison of analytic radius and numerical radius aspect to scaled time τ. (b) Snapshots of zero level contour of numerical solutions

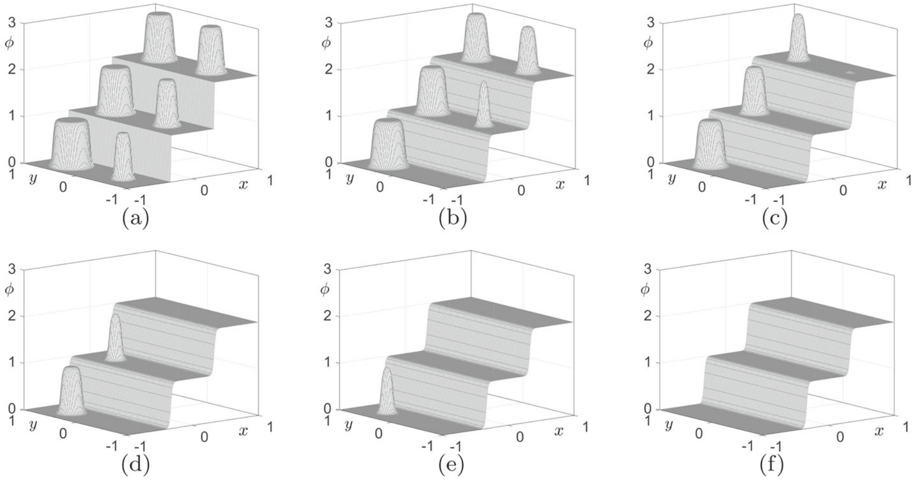

Fig. 11 Snapshots at **a** $t = 0$, **b**($t = 240\Delta t$, **c** $t = 480\Delta t$, **d** $t = 720\Delta t$, **e** $t = 960\Delta t$, and **f** $t = 1200\Delta t$

where R_0 is an initial radius, $R_0 = 0.4$ with $m = 5$ and time step $\Delta\tau = 20\epsilon h^2$. Then we compare the analytic radius and numerical radius. Referring to [9], the analytic radius is given as $R(\tau) = \sqrt{R_0^2 - 2\tau}$ over time. And the numerical radius can be obtained as the average of distances from the center of the zero level points of the numerical solution.

In Fig. 11, the cylindrical shape is considered as an initial condition in which the heights from ground are 1 and the radii are 0.1, 0.125, 0.15, 0.175, 0.2, and 0.225 in the order from the smallest to the largest. The interfaces shrink by the mean curvature flow.

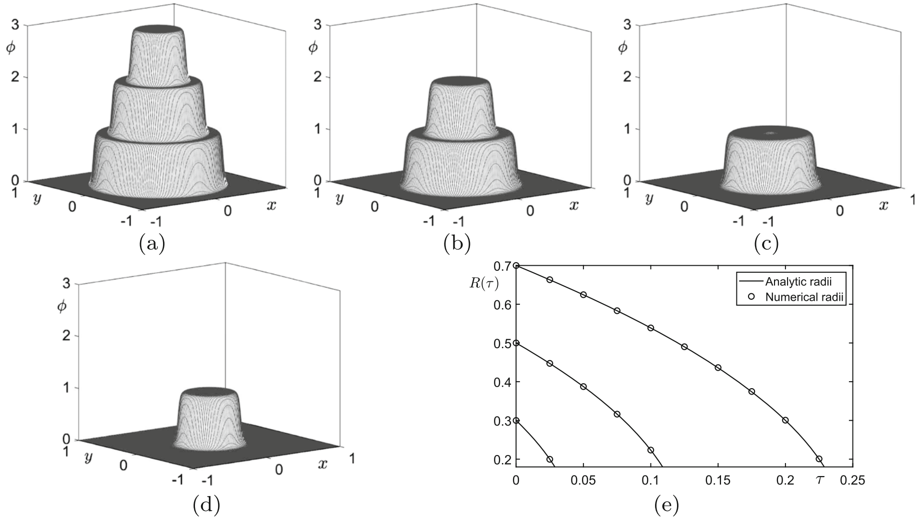

Fig. 12 Snapshots at **a** $t = 0$, **b** $t = 2668\Delta\tau$, **c** $t = 5336\Delta\tau$, and **d** $t = 8004\Delta\tau$. **e** Temporal evolution of numerical and analytic radii

We consider the initial condition of a tower shape with different radii depending on the height as follows:

$$\begin{aligned} u(0,x,y) =& 0.5\left(\tanh\frac{0.7-\sqrt{x^2+y^2}}{0.02}+1\right)+0.5\left(\tanh\frac{0.5-\sqrt{x^2+y^2}}{0.02}+1\right) \\ &+,\ 0.5\left(\tanh\frac{0.3-\sqrt{x^2+y^2}}{0.02}+1\right). \end{aligned} \tag{44}$$

The initial condition (44) is illustrated in Fig. 12(a). The radii are 0.7, 0.5, 0.3 from the bottom. As shown in Fig. 12, the interfaces shrink by the mean curvature flow.

5 Conclusions

In this article, we presented the numerical algorithm of the solution for the gradient flow of MM functional using the operator splitting method. Our scheme is given by the Fourier spectral method for the linear operator and discretized analytic solution of Eq. (8) for the nonlinear operator. We presented that our proposed scheme is unconditionally stable and pointwise boundedness of the numerical solution for any time step. We figure out the effect of parameter ϵ and the corresponding gradient flow of MM functional. Furthermore, we performed several numerical experiments such as motion by mean curvature, second-order accuracy, and stability test. Through the various numerical tests, we presented that our numerical method has unconditionally stable and second-order accuracy. In [15], the convergence of Strang-type splitting for the Allen-Cahn equation was proved. The gradient flow equation of the MM functional is also the Allen–Cahn-type equation, which has a linear Laplacian operator term and a nonlinear double-well potential term. Although we cannot straightforwardly apply the proof in [15] to our model, we will rigorously investigate the error estimates for the proposed method in future work.

Acknowledgements The first author (S. Ham) was supported by the National Research Foundation (NRF), Korea, under project BK21 FOUR. The corresponding author (J.S. Kim) expresses thanks for the support from the BK21 FOUR program. The authors would like to thank the reviewers for their useful comments and suggestions that helped to improve the paper.

Funding The authors have not disclosed any funding.

Data Availability Enquiries about data availability should be directed to the authors.

Conflict of interest The authors declare that they have no conflict of interest.

References

1. Du, Q., Feng, X.: The phase field method for geometric moving interfaces and their numerical approximations. Handb. Numer. Anal. **21**, 425–508 (2020)
2. Garcia-Cardona, C., Merkurjev, E., Bertozzi, A.L., Flenner, A., Percus, A.G.: Multiclass data segmentation using diffuse interface methods on graphs. IEEE Trans. Pattern Anal. Mach. Intell. **36**(8), 1600–1613 (2014)
3. Giga, Y., Okamoto, J., Uesaka, M.: A finer singular limit of a single-well Modica-Mortola functional and its applications to the Kobayashi-Warren-Carter energy. Adv. Calc. Var. **16**(1), 163–82 (2021)
4. Gong, Y., Zhao, J., Wang, Q.: An energy stable algorithm for a quasi-incompressible hydrodynamic phase-field model of viscous fluid mixtures with variable densities and viscosities. Comput. Phys. Commun. **219**, 20–34 (2017)
5. Gong, Y., Zhao, J., Wang, Q.: Second order fully discrete energy stable methods on staggered grids for hydrodynamic phase field models of binary viscous fluids. SIAM J. Sci. Comput. **40**(2), B528–B553 (2018)
6. Ham, S., Hwang, Y., Kwak, S., Kim, J.: Unconditionally stable second-order accurate scheme for a parabolic sine-Gordon equation. AIP Adv. **12**(2), 025203 (2022)
7. Hötzer, J., Reiter, A., Hierl, H., Steinmetz, P., Selzer, M., Nestler, B.: The parallel multi-physics phase-field framework Pace3D. J. Comput. Sci. **26**, 1–12 (2018)
8. Jin, B., Xu, Y.: Adaptive reconstruction for electrical impedance tomography with a piecewise constant conductivity. Inverse Probl. **36**(1), 014003 (2019)
9. Jeong, D., Kim, J.: An explicit hybrid finite difference scheme for the Allen-Cahn equation. J. Comput. Appl. Math. **340**, 247–255 (2018)
10. Jung, Y.M., Kang, S.H., Shen, J.: Multiphase image segmentation via Modica-Mortola phase transition. SIAM J. Appl. Math. **67**(5), 1213–1232 (2007)
11. Kim, H., Yun, A., Yoon, S., Lee, C., Park, J., Kim, J.: Pattern formation in reaction-diffusion systems on evolving surfaces. Comput. Math. Appl. **80**, 2019–2028 (2020)
12. Lee, H.G.: A semi-analytical Fourier spectral method for the Swift-Hohenberg equation. Comput. Math. Appl. **74**(8), 1885–1896 (2017)
13. Lee, H.G., Shin, J., Lee, J.Y.: Energy quadratization Runge-Kutta scheme for the conservative Allen-Cah equation with a nonlocal Lagrange multiplier. Appl. Math. Lett. **132**, 108161 (2022)
14. Li, C., Huang, Y., Yi, N.: An unconditionally energy stable second order finite element method for solving the Allen-Cahn equation. J. Comput. Appl. Math. **353**, 38–48 (2019)
15. Li, D., Quan, C., Xu, J.: Stability and convergence of strang splitting. Part I: Scalar Allen-Cahn equation. J. Comput. Phys. **458**, 111087 (2022)
16. Li, Y., Yoon, S., Wang, J., Park, J., Kim, S., Lee, C., Kim, J.: Fast and efficient numerical finite difference method for multiphase image segmentation. Math. Probl. Eng. **2021**, 1–23 (2021)
17. Li, Y., Kim, J.: Multiphase image segmentation using a phase-field model. Comput. Math. Appl. **62**(2), 737–745 (2011)
18. Ma, R., Sun, W.: FFT-based solver for higher-order and multi-phase-field fracture models applied to strongly anisotropic brittle materials. Comput. Meth. Appl. Mech. Eng. **362**, 112781 (2020)
19. Meny, J., Rumpf, M., Sassen, J.: A phase-field approach to variational hierarchical surface segmentation. Comput. Aided Geom. Des. **89**, 102025 (2021)

20. Wang, Q., Zhang, G., Li, Y., Hong, Z., Wang, D., Shi, S.: Application of phase-field method in rechargeable batteries. Npj Comput. Mater. **6**(1), 1–8 (2020)
21. Rong, Z., Wang, L.L., Tai, X.C.: Adaptive wavelet collocation methods for image segmentation using TV-Allen-Cahn type models. Adv. Comput. Math. **38**(1), 101–131 (2013)
22. Zhao, X., Wang, Q.: A second order fully-discrete linear energy stable scheme for a binary compressible viscous fluid model. J. Comput. Phys. **395**, 382–409 (2019)
23. Zhang, C., Ouyang, J., Wang, X., Chai, Y., Ma, M.: Analysis of the energy stability for stabilized semi-implicit schemes of the functionalized Cahn-Hilliard Mass-conserving gradient flow equation. J. Sci. Comput. **87**(1), 1–25 (2021)
24. Zheng, N., Li, X.: Error analysis of the SAV Fourier-spectral method for the Cahn-Hilliard-Hele-Shaw system. Adv. Comput. Math. **47**(5), 1–27 (2021)